Journal Pre-proof

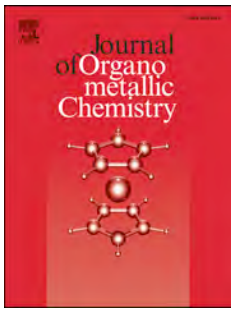

Influence of graphene sheet properties as supports of iridium-based N-heterocyclic carbene hybrid materials for water oxidation electrocatalysis

Beatriz Sánchez-Page, Ana M. Pérez-Mas, María González-Ingelmo, Laura González, Zoraida González, M. Victoria Jiménez, Jesús J. Pérez-Torrente, Javier Blasco, Gloria Subías, Patricia Álvarez, Marcos Granda, Rosa Menéndez

PII: S0022-328X(20)30236-9

DOI: https://doi.org/10.1016/j.jorganchem.2020.121334

Reference: JOM 121334

To appear in: *Journal of Organometallic Chemistry*

Received Date: 1 February 2020

Revised Date: 22 April 2020

Accepted Date: 1 May 2020

Please cite this article as: B. Sánchez-Page, A.M. Pérez-Mas, Marí. González-Ingelmo, L. González, Z. González, M.V. Jiménez, Jesú.J. Pérez-Torrente, J. Blasco, G. Subías, P. Álvarez, M. Granda, R. Menéndez, Influence of graphene sheet properties as supports of iridium-based N-heterocyclic carbene hybrid materials for water oxidation electrocatalysis, *Journal of Organometallic Chemistry* (2020), doi: https://doi.org/10.1016/j.jorganchem.2020.121334.

Influence of graphene sheet properties as supports of Iridium-based N-heterocyclic carbene hybrid materials for water oxidation electrocatalysis

Beatriz Sánchez-Page,[a] Ana M. Pérez-Mas,[b] María González-Ingelmo,[b] Laura González,[b] Zoraida González, M. Victoria Jiménez,[a] Jesús J. Pérez-Torrente,[a] Javier Blasco,[c] Gloria Subías,[c] Patricia Álvarez,[a*]Marcos Granda,[a] and Rosa Menéndez.[a]*

[a] Departamento de Química Inorgánica, Instituto de Síntesis Química y Catálisis Homogénea-ISQCH, Universidad de Zaragoza-CSIC, 50009-Zaragoza, Spain.

[b] Instituto de Ciencia y Tecnología del Carbono, INCAR-CSIC. Francisco Pintado Fe, 26. 33011 Oviedo, Spain.

[c] Instituto de Ciencia de Materiales de Aragón-ICMA, Departamento de Física de la Materia Condensada, CSIC-Universidad de Zaragoza, 50009 Zaragoza, Spain.

Dedicated to Professor Dr. F. Ekkehardt Hahn on the occasion of his 65th birthday

ABSTRACT.

The effect of the structural properties of graphene materials on the local structure of -OH anchored Ir(I)-NHC complexes is herein investigated. For that, two partially reduced graphene oxides exhibiting different sheet properties due to an adequate selection of the crystalline characteristics of their parent graphite were used. The main differences among them were the size of Csp^2 domains within their graphenic layers and the distribution of functional groups at the basal planes and edges. Anchoring of N-methylimidazolium moieties through the graphene -OH functional groups and subsequent formation of the Ir(I)-NHC complexes resulted in the formation of graphene-based hybrid materials. The structural differences of the support have an influence in the interaction of the supported iridium compounds with the graphene sheet. The oxygenated functional groups in the material with a smaller graphene sheet are closer leaving larger Csp^2 domains in the graphene layer, favoring their interaction with the supported iridium atoms therefore displacing the chlorido ligand from the first coordination shell. In contrast, the hybrid material in which the distribution of the oxygenated functional groups within the basal planes of the graphenic layer is more homogeneous shows partial chlorido displacement. This fact has an influence on the electrocatalytic performance of the iridium-based hybrid materials as water oxidation catalysts (WOCs), exhibiting improved catalytic activity and the catalyst having coordinated chlorido ligands.

Keywords: water oxidation, graphene supports, iridium, N-heterocyclic carbenes (NHC).

INTRODUCTION

Nowadays, global warming and depletion of fossil fuels have become a major challenge considering the growing worldwide energy demand [1]. Within this scenario, it became a critical issue to progress towards a more sustainable society moving towards more efficient renewable energies. The use of solar energy in combination with water electrolysis and CO_2 reduction are key processes to produce chemical fuels, being therefore efficient renewable energy storage systems. However, the large over-potential and slow kinetics of the oxygen evolution reaction (OER) has made catalytic water oxidation a major challenge for the later decades [2,3].

Among the most efficient water oxidation catalysts (WOC) are those based on Ru and Ir [4,5,6]. Moreover, homogeneous catalysts based on these metals exhibit a high efficiency in the evolution of oxygen and have more tunable structures when compared to those of heterogeneous systems such as metal oxides, (oxy)sulfides, (oxy)nitrides or metal (oxy)nanoparticles [7,8,9]. However, for a large-scale utilization of these homogeneous catalysts, their immobilization on the surface of heterogeneous electrodes, particularly via covalent attachment, is required since it substantially improves their recyclability, reduces the amount of catalyst, enhances their efficiency and robustness, and prevents deactivation via associative intermolecular pathways [10,11]. Carbon materials are commonly used for developing heterogeneous WOCs [12,13,14,15]. Among them, graphene offers additional advantages that could promote a proactive role improving catalytic efficiency, as for example, a unique electronic behavior, high surface area or outstanding chemical stability [16,17]. The graphene materials produced from graphite by the easily scalable chemical route –i.e. via oxidation of graphite to produce graphene oxides (GOs) and/or subsequent reduction

to produce partially reduced graphene oxides (RGOs)– are versatile materials which exhibit in their structure a series of oxygenated functional groups from which the organometallic catalyst can be covalently attached. Moreover, this route offers the possibility to selectively control the structural properties of the obtained graphene materials. Thus, it is possible to modulate the type and amount of oxygenated functional groups located at basal planes and edges of GO sheets by selecting the oxidation method [18] or selectively remove certain functional groups during the production of TRGOs [19]. Even further, the type and distribution of oxygenated functional groups in the GO can be also modulated by an adequate selection of the crystallinity of the parent graphite [20,21]. This versatility in processing allows graphene materials with different structure and properties to be obtained, a fact which has been used to improve their field of application (e.g. electrochemical systems, composites, etc.) [22,23]. Catalytic applications are not an exception and there are a great number of studies in which graphene materials act as proactive supports of nanoparticles [24] or even organometallic compounds [25] in different catalytic systems [17,26].

Much more scarce are the studies focused on the graphene properties themselves and the influence of their structural properties on the catalytic performance of the resulting supported hybrid catalytic systems, being most of them centered in studying the effect of graphene sheet reduction. As an example, the positive correlation between hydrogen transfer catalytic activity of iridium N-heterocyclic carbene (NHC) organometallic complexes supported onto GO and TRGO has been recently reported [27].

Bearing this in mind, herein two TRGOs, obtained from two graphites of different crystallinity, have been prepared for the covalent anchorage of an organometallic Ir(I)-NHC complex. This anchorage, the same for the two TRGOs, includes a sequential and specific reaction with the graphene -OH functional groups that gives rise to the supported iridium complexes [28]. The properties of the parent graphenes and hybrid materials have been

extensively studied by means of XPS, Raman and EXAFS techniques, and the electrocatalytic water oxidation behavior of the supported iridium catalysts evaluated. Moreover, the objective of this work is double; on one hand it is intended to determine if structural sheet properties lead to some structural changes in the first coordination sphere of the anchored metal compounds and, on the other hand, to determine if these changes lead to different water oxidation catalytic behavior. Interestingly, a correlation has been found between the properties of the parent graphene sheets and the iridium local structure in the supported catalysts which also affect the catalytic performance.

2. EXPERIMENTAL SECTION

2.1. Materials

Two graphites were used in this work as graphene oxide precursors. These graphites were obtained from coal-derived samples, coal tar for **G-1** and anthracene oil for **G-2**, by successive thermal polymerization, carbonization and graphitization to 2700°C.

The imidazolium salt [MeImH$(CH_2)_3$OH]Cl and the starting organometallic compound [Ir(μ-OMe)(cod)]$_2$ were prepared according to standard literature procedures [29, 30]. All other chemicals were purchased from Aldrich. HPLC grade reagents were employed in all the experiments. Solvents were distilled immediately prior to use from the appropriate drying agents or obtained from a Solvent Purification System (Innovative Technologies).

2.2. Preparation of thermally reduced graphene oxides

Thermally reduced graphene oxides (TRGOs) were obtained from the two graphites by means of a modified Hummers process that involves two consecutive steps [19]: (i) oxidation of graphite to graphite oxide (**GO-1** and **GO-2**), and (ii) thermal treatment at 500ºC in a horizontal furnace under a nitrogen flow of 50 mL min^{-1}. The residence time at the final

temperature was 60 min. TRGOs were labeled, according to the graphite precursor, as **TRGO-1** and **TRGO-2**.

2.3. Preparation of graphene supported hybrid catalysts.

TRGO-1 and **TRGO-2** were functionalized with the imidazolium salts following a three-steps procedure. First, 0.100 g of **TRGO-x** were dispersed in 20 mL of anhydrous dichloromethane (DCM). Then, p-nitrophenylchloroformate (3.02 g, 15.0 mmol) and triethylamine (2.1 mL, 15.0 mmol) were added under inert atmosphere. The mixture was cooled to 0 ºC with an ice bath and stirred for 24 h, letting the temperature slowly reach 20 ºC. The resultant solid was filtered, washed three times with DCM (20 mL), and dried for 2 h under vacuum. The solid was dispersed in 15 mL of anhydrous tetrahydrofuran (THF) under a nitrogen atmosphere and then, the imidazolium salt [MeImH$(CH_2)_3$OH]Cl (0.070 mg, 0.392 mmol) and a catalytic amount of triethylamine (0.2 mL) were added and the mixture refluxed for 24 h. The dispersion was filtered and the solid was washed with THF (3 x 20 mL) and DCM (3 x 20 mL) and then dried at 100 ºC in a preheated furnace overnight. These materials were labelled as **TRGO-1-Ir** and **TRGO-2-Ir** depending on the parent graphite used.

2.4. Scientific equipment. Characterization of supports and hybrid catalysts.

High-resolution transmission electron microscopy (HRTEM) images were obtained using a JEOL JEM-2100F transmission electron microscope equipped with a field-emission-gun (FEG) operating at 200 kV. Energy-dispersive X-ray spectroscopy (EDX) was used to verify the atomic composition of the hybrid catalyst. Elemental analyses were performed on a LECO-CHNS-932 micro-analyser and a LECO-VTF-900 furnace coupled to the micro-analyser. X-ray photoelectron spectroscopy (XPS) spectra were performed on a SPECS system operating under a pressure of 10^{-7} Pa with a Mg Kα X-ray source. The functional groups in the graphene-based materials were quantified by deconvolution of the

corresponding high resolution XPS peaks using a peak analysis procedure that employs a combination of Gaussian and Lorentzian functions and a Shirley baseline [31]. The spectra did not require charge neutralization and were subsequently calibrated to the C1s line at 284.5 eV. The binding energy profiles for the C1s spectra were deconvoluted as follows: undamaged structures of Csp^2-hybridized carbons (284.5 eV), damaged structures or Csp^3-hybridized carbons (285.5 eV), C-OH groups (286.5 eV), O-C-O functional groups (287.7 eV) and C(O)OH groups at 288.7 eV. The amount of iridium in the hybrid catalysts was determined by means of Inductively Coupled Plasma Mass Spectrometry (ICP-MS) in an Agilent 7700x instrument [32]. Raman spectroscopy was performed on a Renishaw 2000 Confocal Raman Microprobe (Rhenishaw Instruments, England) using a 514.5 nm argon ion laser. Spectra were recorded from 750 to 3500 cm^{-1}. Room temperature X-ray absorption spectroscopy (XAS) measurements at the Ir L_3-edge were carried out using a Si (311) double crystal monochromator at the CLAESS beam line [33] of the ALBA synchrotron facility (Cerdanyola del Vallès, Spain). The XAS spectra were measured in the transmission mode using pellets diluted with cellulose, if necessary, in order to optimize the absorption jump. The energy resolution $\Delta E/E$ was estimated to be about 8×10^{-5} at the Ir L_3-edge, and a pellet of Ir metal mixed with cellulose was simultaneously measured for energy calibration. The XAS spectra were normalized to unity edge jump and the

k-weighted Extended X-ray Absorption Fine Structure (EXAFS) spectra, $k^2\chi(k)$, were obtained using the Athena software from the Demeter package [34]. The Fourier Transform (FT) curves of the $k^2\chi(k)$ signals were obtained for the $2.85 \leq k \leq 14.5$ $Å^{-1}$ range, using a sinus window. The EXAFS spectra were analyzed using theoretical phases and amplitudes calculated by the FEFF-6 code [35] and fits to the experimental data were performed in R-space (between 1.15 and 3.95 Å) with the ARTEMIS program of the Demeter package.

2.5. Electrochemical measurements.

Electrodes were prepared as follows: 5 mg approximately of **TRGO-X-Ir** (as active material) were diluted in EtOH (5 mL) and subsequently drop-casted onto a graphite disk current collector (2 cm^2) and dried at 80 °C (1 h) in order to remove the solvent. Cyclic voltammetry (CV) and chronoamperometry (CA) experiments were performed in a Teflon home-made three-electrode cell at room temperature and under inert atmosphere. The cell consisted on the previously prepared **TRGO-X-Ir** electrodes as the working electrodes (1 cm^2 of exposed area), Ag/AgCl/3.5 M KCl as the reference electrode and a graphite rod as the counter electrode. All the potentials reported in this study were referenced to Ag/AgCl/3.5 M KCl (i.e., 0.205 V *vs.* NHE). The supporting electrolyte consisted of a 1.0 M phosphate buffer solution (PBS) at pH 7.0. The electrochemical measurements were performed on a BioLogic VMP Multichannel Potentiostat. The current density values were calculated after background subtraction of the bare **TRGO-X** electrode. The evolution of oxygen was measured at the headspace of the electrocatalytic cell by using a HP 5890 gas chromatograph fitted with a thermal conductivity detector (TCD) and packed columns (Porapak N and molecular sieve). Mixtures of gases of known composition were used for the quantitative analysis.

RESULTS AND DISCUSSION

Properties of parent thermally reduced graphene oxides (TRGO).

With the aim of studying the influence of the graphene structure on the catalytic behavior of supported Ir–NHC hybrid catalysts, two thermally reduced graphene oxides (**TRGO-X**, X = 1 and 2) were selected as catalyst support. They were prepared from two graphites (**G-1** and **G-2**) with different crystalline structure. **G-1** exhibits a more compact graphitic structure than **G-2**, as observed by the higher Lc value (51 vs 15) and slightly shorter interlayer distance

(d_{002}, 0.336 vs 0.337), measured by means of XRD analysis (Table 1). Consequently, after subjecting these samples to a modified Hummer´s method (see Supplementary data), the resultant graphite oxide from **G-1** (**GO-1**) presents higher amount of oxygen in its structure (55.8 wt.% compared to 52.8 wt.% in **GO-2**), as determined by elemental analysis. The higher interlayer distance in this sample (0.949 *vs* 0.915 nm for **GO-1** and **GO-2**, respectively) suggests a location of the functional groups at the basal planes of the graphenic layers. It is also interesting to mention that the lateral size of the graphene oxide sheets prepared from **GO-1** by sonication (see Supplementary data) (~450 nm) is slightly larger than that from **GO-2** obtained under the same experimental conditions (~300 nm).

Table 1. Main characteristics of parent graphites **(G-X)**, graphite oxides **(GO-X)** and thermally reduced graphene oxides **(TRGO-X)** (X=1,2)

Sample	Elemental analysis (wt.%)				Raman	XRD	
	C	H	O	C/O[a]	I_d/I_g[b]	d_{002}[c]	L_c[d]
G-1	99.9	0.1	0.0	-	-	0.336	51
G-2	99.9	0.1	0.0	-	-	0.337	15
GO-1	40.7	3.3	55.8	1.0	-	0.949	-
GO-2	43.7	2.4	52.8	1.1	-	0.915	-
TRGO-1	79.9	0.7	19.2	5.5	0.95	-	-
TRGO-2	83.5	0.7	15.8	7.0	0.93	-	-

[a] Carbon/oxygen atomic ratio; [b] Intensity ratio of D and G bands; [c] Interlayer distance (nm); [d] Crystal size in the c-direction (nm)

These structural differences are, at some extent, retained after their thermal treatment at 500 ºC to produce the **TRGOs** via simultaneous exfoliation and reduction steps (see Supplementary data). Elemental analysis measurements suggest that, despite that the reduction process significantly diminishes the oxygen content in both partially reduced graphene materials (from ~52-55 wt.% in **GOs** to ~15-20 wt.% in **TRGOs**), the graphene sheet from **GO-1** (**TRGO-1**) is more oxidized than **TRGO-2** (lower C/O ratio, 5.5 vs 7.0 for

TRGO-2, Table 1). As determined by means of XPS C1s (Table 2), this is mainly a consequence of the formation of larger number of C-O bonds along the basal plane of the sheets, while **TRGO-2** exhibit more functional groups at the edges or defects of the sheets (C=O or COO bonds), which could be related with its smaller sheet size. This analysis also reveals that the remaining carbon atoms in **TRGO-1** are less aromatic (72.3 % of Csp^2 and 13.7 % Csp^3 vs 77.4 % Csp^2 and 10.0% Csp^3 in **TRGO-2**). Moreover, the full width at half maximum (FWHM) of the Csp^2 band is also higher in **TRGO-1** (1.4 eV vs 1.2 eV in **TRGO-2**), which suggests that the differences among samples are not only the number of functional groups in the sheets but also a more heterogeneous environment of the carbon atoms within the graphene basal plane. This fact was further corroborated by means of Raman determinations in which the bands measured are only associated to defective graphene regions (that is, to defects participating in the double resonance Raman scattering near K point of Brillouin zone) [36]. Thus, both **TRGOs** exhibit the typical Raman profile of partially reduced graphene materials (see Supplementary data) with two main prominent peaks assigned to G band (~1590 cm^{-1}) and D band (~1350 cm^{-1}). However, the higher I_D/I_G ratio of **TRGO-1** (0.95 vs 0.93 in **TRGO-2**, Table 1) are in agreement with a larger size of the Csp^2 domains within the basal planes in **TRGO-2** sheet while in **TRGO-1** the graphitic domains are more disrupted with C=C/C-H vibrations of segments at grain boundaries, that is, carbonaceous graphenic structure with more defects such as holes or vacant within the basal planes. Gathering the available data, the overall structure of both samples could be understood as follows: **TRGO-1** (from the graphite with larger crystal size) seems to be composed by graphenic sheets of larger size in which the remaining functional groups (mainly epoxy groups) are homogeneously distributed along the basal planes largely disrupting its graphenic structure. On the other hand, the sheet size of **TRGO-2** (from the graphite with lower crystal size) is smaller and contains more oxygenanted functional groups

located at the edges or holes of the sheets while the oxygenated functional groups and defects at the basal planes (epoxy groups) could be closer among them, leaving Csp^2 domains of larger size within the basal planes (Chart 1). These results are fully consistent with those previously reported concerning the preparation and characterization of GOs from graphites of different crystallinity [21].

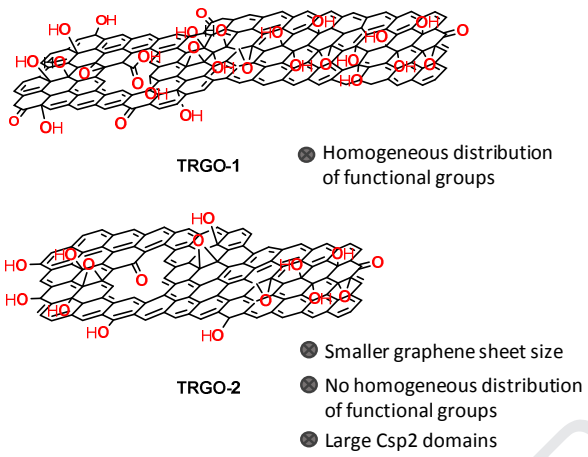

Chart 1. Proposed structure of parent thermally reduced graphene oxides.

Preparation and characterization of two graphene-based Iridium–NHC hybrid catalysts.

The supported graphene-based Ir–NHC hybrid catalysts were prepared form the two **TRGO-X** by means of a procedure recently described by the authors (Fig. 1) [28]. Briefly, the multiple steps procedure comprises the initial selective reactivity of the -OH groups in the graphene sheet with p-nitrophenylchloroformate leading to the corresponding p-nitrophenyl carbonate esters [37,38]. In a second step, treatment of the carbonates with the imidazolium salt $[MeImH(CH_2)_3OH]Cl$ resulted in the displacement of the p-nitrophenol with formation of the imidazolium functionalized graphene materials that, after reaction with the methoxo iridium(I) dimer compound $[Ir(\mu\text{-}OMe)(cod)]_2$ (cod = 1,5-cyclooctadiene) afforded the hybrid

materials, **TRGO-1-Ir** and **TRGO-2-Ir**, featuring supported Ir-NHC complexes covalently bonded through carbonate functions.

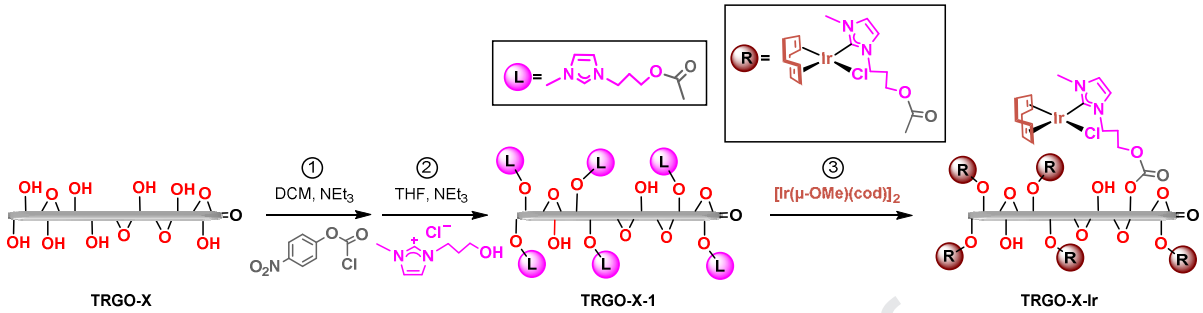

Fig. 1. Preparation procedure of **TRGO-X-Ir** graphene-based Ir–NHC hybrid materials (X = 1 or 2 for both **TRGO-1** or **TRGO-2** parent materials, respectively).

XPS analysis of both **TRGO-X-Ir** samples revealed the presence of Ir in a similar amount (0.8-1.1 %). The high resolution Ir4f XPS spectra (Fig. 2a) show, for both samples, the expected two peaks (corresponding to $Ir4f_{5/2}$ and $Ir4f_{7/2}$) centered at 65.5 eV and 62.4-62.5 eV, which are characteristics of iridium(I) compounds [39]. The small differences in the maximum value of the Ir 4f7/2 band of both compounds could be related with some differences in the first coordination shell of their iridium atoms.

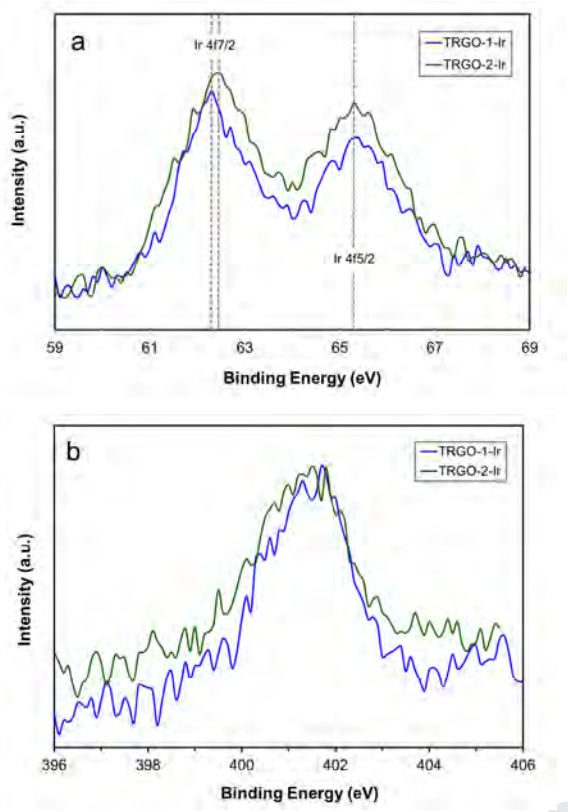

Fig. 2. High resolution XPS a) Ir4f and b) N1s core level curves of hybrid materials **TRGO-1-Ir** and **TRGO-2-Ir**.

HRTEM images of **TRGO-1-Ir** and **TRGO-2-Ir** (Fig. 3a,b respectively) showed the homogeneous distribution of the electrondense regions corresponding to the iridium (diameters from 0.2 to 0.7 nm) and to clusters or nanoparticles possibly formed during beam irradiation (spots or larger diameter) [40]. Interestingly, the higher aromaticity of **TRGO-2-Ir** observed by Raman analysis was also observed in the image of this sample, in which highly crystalline regions within the basal planes are visible (see Fig. 3b and expanded inset). EDX mapping of the HRTEM regions obtained for **TRGO-1-Ir** (Fig. 3c,d,e) and **TRGO-2-Ir** (see Supplementary data) confirms the presence of nitrogen (Fig. 3e) and iridium (Fig. 3d) being homogeneously distributed within the carbonaceous lattice.

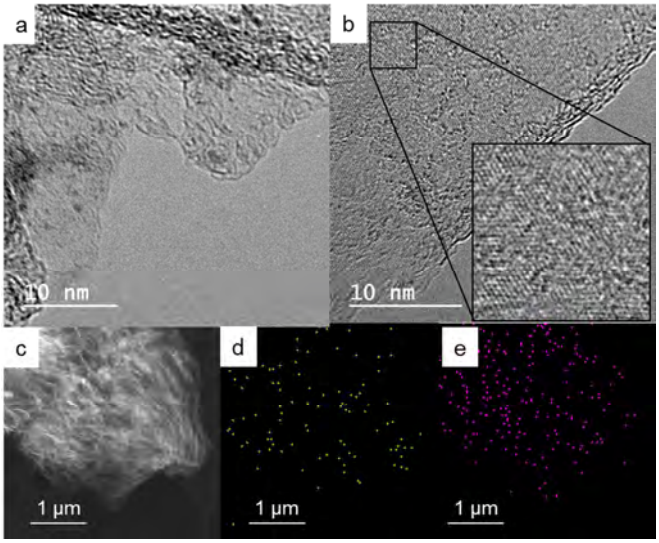

Fig. 3. HRTEM images of a) **TRGO-1-Ir** and b) **TRGO-2-Ir**. c) EDX image of **TRGO-1-Ir**, d) nitrogen mapping and e) iridium mapping extracted from EDX analysis.

The XPS atomic nitrogen content for **TRGO-2-Ir** is of 1.6 % with a Ir/N ratio of 0.8/1.6, that is, the expected for quantitative formation of the Ir-NHC complexes. This ratio in **TRGO-1-Ir** is 1.1/2.4 which indicates a slightly lower degree of functionalization in the last metalation step of the synthetic procedure. The XPS N1s spectra of both samples are quite similar and show the expected patterns for the N-heterocyclic moiety as a broad signal at 401.4 eV (Fig. 2b). The deconvolution of the XPS C1s spectra of these hybrid materials also show an increased intensity of the C-O/C-N peaks (Table 2) with respect to the parent graphene samples, as expected for the presence of the NHC ligand. Moreover, this band is of higher intensity in **TRGO-1-Ir** which is in agreement with the higher functionalization of this sample, while **TRGO-2-Ir** shows a larger number of COO bonds. All these results evidences not only the larger N-functionalization of the **TRGO-1-Ir** graphene sheets but also the presence of non-deprotonated imidazolium groups after reaction with the dinuclear iridium precursor, being this reaction almost quantitative for **TRGO-2-Ir**.

Table 2. XPS data of thermally reduced graphene oxides **(TRGO-X)** and graphene supported Ir(I)-NHC complexes **(TRGO-X-Ir)**.

Sample	Csp^2 % (FWHM[a])	Csp^3 % (FWHM[a])	C-O C-N % (FWHM[a])	C=O % (FWHM[a])	COO % (FWHM[a])	Ir %	N %
TRGO-1	72.3 (1.4)	13.7 (1.1)	9.5 (1.2)	2.7 (1.1)	1.8 (1.1)	-	-
TRGO-2	77.4 (1.2)	10.0 (1.1)	7.0 (1.1)	3.6 (1.1)	2.0 (1.1)	-	-
TRGO-1-Ir	61.9 (1.4)	12.3 (1.1)	17.0 (1.1)	5.8 (1.1)	3.0 (1.2)	1.1	2.4
TRGO-2-Ir	64.3 (1.3)	12.5 (1.1)	12.8 (1.2)	5.3 (1.1)	5.0 (1.3)	0.8	1.6

[a] FWHM in eV

The local structure of the Ir complexes was studied by means of EXAFS analysis. The FT of **TRGO-1-Ir** and **TRGO-2-Ir** samples are compared in Fig. 4a. The main difference is seen in the most intense peak of the FT curves corresponding to the first coordination shell. **TRGO-2-Ir** exhibits a strong peak at R **≈** 1.65 Å (without phase shift correction) which is characteristic of the bond distance between an atom of Ir and a light element such as C or O [40, 41]. This peak is less intense for the **TRGO-1-Ir** sample and it is accompanied by a shoulder at higher R-values that reminds the contribution from Ir-Cl paths in related compounds [40,41]. Beyond this peak, both FT curves show the same features for both hybrid materials. The real part of the Fourier filtered spectra between 1.15 and 3.95 Å is shown in the Fig. 4b. Here, the difference between both samples is clearly manifested in the interference observed at k **≈** 8-9 $Å^{-1}$ for **TRGO-1-Ir** that is lacked in the spectrum of **TRGO-2-Ir**. Such interference is also typical of the occurrence of Ir-Cl bond length in related compounds [41].

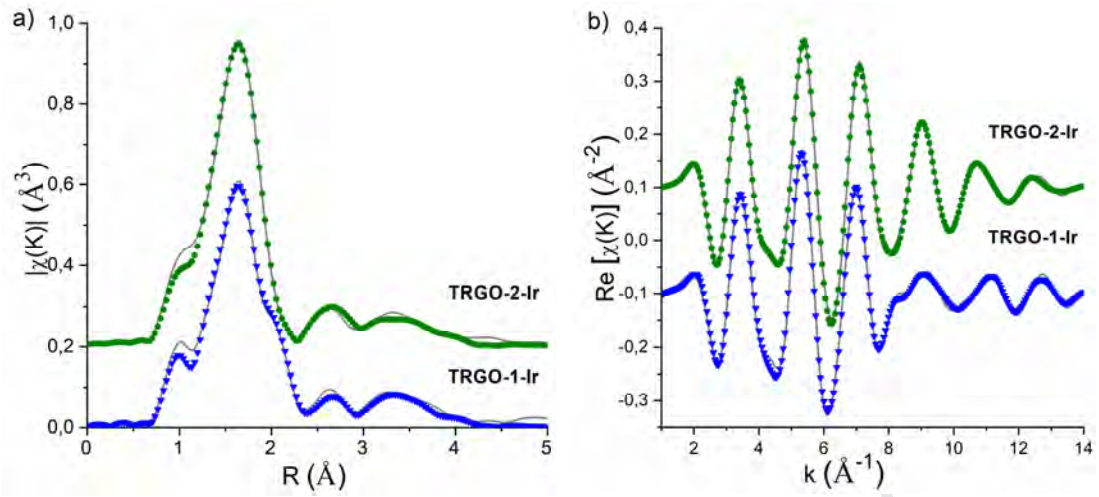

Fig. 4. a) Fits (lines) of the Fourier transform signal from the k^2-weighted EXAFS signal (triangles and circles) of **TRGO-2-Ir** and **TRGO-1-Ir** until R = 3.95 Å. b) Fits (lines) of the real part of the Fourier-filtered spectra (triangles and circles) between R = 1.15–3.95 Å for the same samples in the k-space.

In order to model the Ir local structure in these hybrid compounds, we have used the modified crystallographic data [40] of compound $[Ir(NCCH_3)(cod)\{MeIm(CH_2)_3OH\}][BF_4]$ [41] which is expected to have a similar environment for the Ir atom as it is coordinated to an imidazol-2-ylidene ring, a cyclooctadiene (cod) ligand and a nitrogen atom. The modification consisted of replacing the nitrogen coordinated to the iridium with an oxygen and thus, we can obtain theoretical phases and amplitudes for Ir-O, Ir-C and Ir-N paths, including multiple scattering paths. The values for the Ir-Cl path were obtained from the reference complex $[IrCl(cod)\{MeIm(CH_2)_3OH\}]$ used in a previous study of carbon nanotubes [41]. The Ir environment in this complex is similar to $[Ir(NCCH_3)(cod)\{MeIm(CH_2)_3OH\}][BF_4]$ with the exchange of a nitrogen for a chlorine atom in the first coordination shell. The EXAFS spectra of **TRGO-2-Ir** can be fitted with the data of modified $[Ir(NCCH_3)(cod)\{MeIm(CH_2)_3OH\}][BF_4]$ indicating that the first coordination shell of Ir in this material is composed by six light elements: an oxygen from the oxidized graphene, four carbons from the cod ligand and a fifth carbon from the imidazol-2-ylidene ligand. Therefore,

the Cl^- present in the imidazolium salt (see Fig. 1) remains uncoordinated after the anchorage process to **TRGO-2** and subsequent metalation (Chart 2). Further coordination shells up to R ≈ 4 Å can be accounted for by the single and multiple scattering contributions arising from cod and imidazol-2-ylidene ligands. The fits in R- and *k*-spaces can also be seen in the Fig. 4. The refined parameters for the first coordination shell are summarized in the table 3.

Table 3. Refined inner potential, interatomic distances and Debye-Waller factors (σ^2) obtained from the best fits.[a,b,c]

Sample	Ir-C(NHC) (Å)	Ir-O (Å) [b]	Ir-C(cod) (Å)	σ^2 (Å^2)[c]	Ir-Cl (Å)	σ^2 (Å^2)[c]	R_F
TRGO-1-Ir	2.029(7)	2.029(7)	4x2.164(15)	0.0065(6)	2.389(13)	0.0037(10)	0.009
TRGO-2-Ir	2.025(23)	2.025(23)	2x2.103(13) 2x2.164(13)	0.0046(14)	-	-	0.005

[a] The residual factor (R_F) accounts for the misfit between the actual data and the theoretical calculations. Numbers in parentheses are the errors estimated in the last significant digits. A single inner potential E_0 was refined for all paths, being E_0=1.9(9) eV for **TRGO-1-Ir** and E_0=2.3(6) eV for **TRGO-2-Ir**. [b] Ir-O bond length was set to the value of Ir-C_1(NHC). [c] A single Debye-Waller factor was refined for Ir-C(NHC), Ir-O and Ir-C_{cod}. The coordination numbers of Ir-O and Ir-Cl paths for the **TRGO-1-Ir** sample were refined from the attenuation factors (S_0^2) as N=S_0^2=0.48(3) and N'=1- S_0^2=0.52(3), respectively. S_0^2 was fixed to 1 for the rest of paths.

Regarding the **TRGO-1-Ir** material, our attempts to fit the spectrum using an environment without removing Cl from the first coordination shell of Ir, *ie* similar to [IrCl(cod){MeIm$(CH_2)_3$OH}] complex with an Ir-Cl path and five Ir-C paths, were unsuccessful as the intensity of the abovementioned shoulder turned out to be too big. The next logical step was to consider a partial replacement of Cl by O. The refinements quickly converged indicating than half of the Cl present in the imidazolium salt is coordinated to iridium while the other half remains uncoordinated due to the replacement with O from the oxidized graphene in the **TRGO-1-Ir** hybrid material. The fit and the refined results can be viewed in Fig. 4 and Table 3, respectively. The results obtained for further shells (not shown here) are similar to those observed in the previous sample indicating a similar distribution of

cod and imidazol-2-ylidene rings around the Ir atoms for both hybrid materials. A possible explanation for these Ir local structural differences could be found considering the previously discussed carbonaceous structure of both graphene sheets (**TRGO-1** and **TRGO-2**). Despite the fact that **TRGO-1** appears to have more oxygenated functional groups (mainly C-O) in its layers, they appear to be more homogeneously distributed along a larger graphene basal plane and possibly less close to each other. In contrast, the oxygenated functional groups in **TRGO-2**, although slightly less abundant, are much closer among them. As the iridium atoms occupies positions coming from the functionalization of -OH groups, they also will be closer to each other and to other free oxygenated functional groups in **TRGO-2-Ir**, possibly favoring additional interaction Ir-graphene and displacing the chlorido ligands (Chart 2).

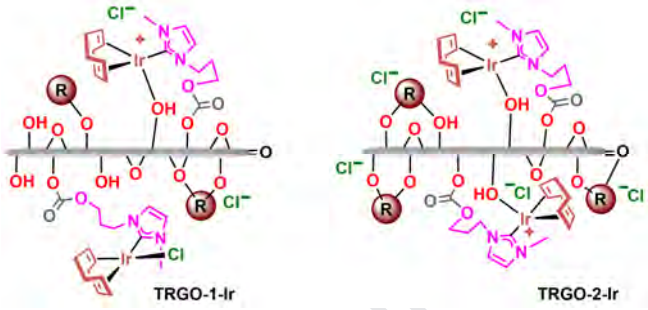

Chart 2. Proposed structure for a) **TRGO-1-Ir** and b) **TRGO-2-Ir** (in accordance with the EXAFS analysis).

Electrocatalytic water oxidation performance of the hybrid catalysts.

In order to study their electrochemical water oxidation behavior, the two graphene-based Iridium–NHC hybrid materials were drop casted onto graphite disks of 1 cm of diameter in order to be used as electrodes to carry on the electrochemical measurements. SEM analysis of the electrode surface (Fig. 5a for **TRGO-1-Ir** electrode) shows the heterogeneous morphology created by the superposition of wrinkled graphene sheets (inset in Fig. 5a). **TRGO-2-Ir** electrode shows a similar appearance (see Supplementary data). The electrodes

were set up in an inert home-made three electrode cell using a Ag/AgCl/3.5 M KCl and a graphite rod, as reference and counter electrodes respectively. A phosphate buffer solution (PBS) at pH of 7.0 was selected as supporting electrolyte for the electrocatalytic tests. The formation of oxygen during the experiments was recorded by means of gas chromatography (No CO or CO_2 formation was detected).

The electrocatalytic performance of the **TRGO-1-Ir** and **TRGO-2-Ir** electrodes was evaluated studied by means of cyclic voltammetry (CV) measurements (Fig. 5b). The corresponding cyclic voltammograms (CVs) were recorded between 0.00 and 1.40 V (*vs* Ag/AgCl/3.5 M KCl, i.e., 0.20 V *vs* NHE). At 1.4 eV (corresponding to an overpotential of 0.79 V over the thermodynamic potential for water oxidation, which is 0.61 V vs Ag/AgCl/3.5 M KCl at pH 7.0), the highest current density was measured for **TRGO-1-Ir** (~22 mA cm^{-2}) while **TRGO-2-Ir** only reaches ~16 mA cm^{-2} at this potential. These data correspond to the second CV recorded. As comparative purposes, the current densities of the bare **TRGO-X** electrodes accounts for less than 3-4 mA cm^{-2} in the first CV recorded, being these values even lower in the second CV used for measurement (see Supplementary data). On the other hand, **TRGO-1-Ir** reaches a current density of 10 mA/cm^2 at 1.15 V while **TRGO-2-Ir** reaches this value at 1.30 V [13,15,42]. Moreover, the Tafel slope obtained for **TRGO-1-Ir** (Fig. 5c) is much lower than that of **TRGO-2-Ir** (185.5 mV dec^{-1} vs 336.8 mV dec^{-1}) which is in agreement with an enhanced kinetics on the former. The amount of iridium in each electrode, calculated by ICP-MS, resulted slightly different (0.00188 and 0.00201 mmol for **TRGO-1-Ir** and **TRGO-2-Ir**, respectively). It was also interesting to compare the current densities measured on each electrode per mmol of Ir (Fig. 5d). The results remarks even more the catalytic efficiency of **TRGO-1-Ir** with respect to that of **TRGO-2-Ir**. Chronoamperometry (CA) experiments were carried out on both electrodes (Fig. 6) measuring simultaneously the evolution of oxygen in both experiments by means of gas

chromatography (Fig. 6, inset). A similar trend was observed in both cases. The current measured was stabilized after 150 s, time from which only a small decay of such current is observed. However, the value of the stabilized current measured on **TRGO-1-Ir** was significantly higher. The, both samples exhibiting a similar trend but confirming the slightly higher catalytic efficiency of **TRGO-1-Ir** in comparison with **TRGO-2-Ir**.

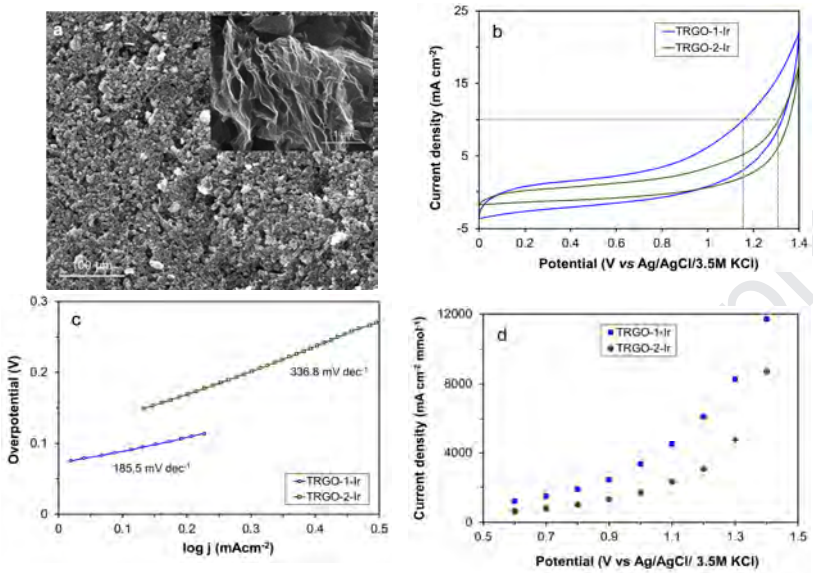

Fig. 5. a) SEM images of **TRGO-1-Ir** electrode, b) CVs recorded on the two electrodes between 0.00 and 1.40 V, c) Tafel plots, d) current density values calculated per mmol of Ir.

Once the experiments ended, a small quantity of Ir in the solution (0.05 % for **TRGO-1-Ir** and 0.3 % for **TRGO-2-Ir**) was detected by ICP-MS and only small differences in the electrode surface were detected after washing (see Supplementary data). Further experiments are ongoing to elucidate the mechanism involved in these catalytic cycles including the changes promoted at the metal center during the catalytic cycle.

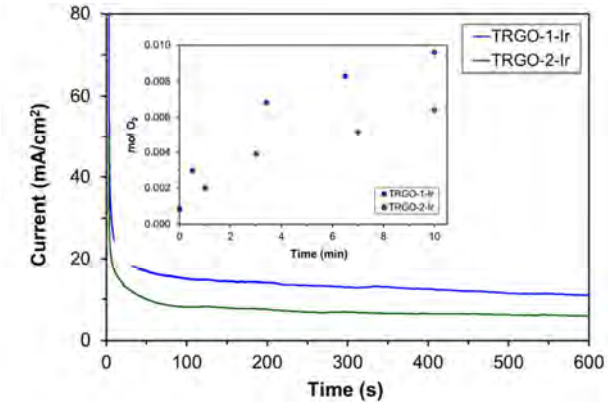

Fig. 6. CAs recorded at an applied potential of 1.4 V on the **TRGO-1-Ir** and **TRGO-2-Ir** electrodes. Inset shows the evolution of oxygen as a function of time during the chronoamperometric measurements as determined by gas chromatography.

All the results obtained suggest that small structural differences in the graphenic support could promote some changes in the first coordination shell of the metal center (catalyst). Moreover, these changes could affect the catalytic behavior of the supported organometallic compound.

Going further in these asseverations, it seems that graphene layers in which the oxygenated functional groups are closer to each other (**TRGO-2**) lead, after the selective covalent attachment of the iridium organometallic compound, to the ionization of the chlorido ligand (otherwise attached directly to the iridium center) by interacting with these oxygenated functional groups. As a consequence, the electrocatalytic activity in water oxidation decay. It seems therefore that the presence of the chlorido ligand in the coordination sphere of the iridium center is somehow required to perform the water oxidation effectively.

Conclusions

We have confirmed that the covalent anchorage of Ir(I)-NHC complexes through carbonate functions to thermally reduced graphene oxides of different properties lead to hybrid

materials suitable as water oxidation electrocatalysts. This work also demonstrates that the structural properties of the graphene layers play a crucial role not only in the overall structure of the supported iridium compounds but also in their subsequent electrocatalytic behavior towards water oxidation. In this sense, it appears that partially reduced graphene layers in which the remaining functional groups are closer to each other (produced when a graphite with small domains is used as parent material in the chemical via) could led to a partial displacement of the chlorido ligand coordinated to the metal center. This seems to have a negative impact in its electrocatalytic behavior in water oxidation.

Declaration of competing interest

The authors declare that they have no known competing financial interests or personal relationships that could have appeared to influence the work reported in this paper.

Acknowledgments

Financial support from the Spanish Ministry of Economy and Competitiveness MINECO/FEDER under the projects CTQ2016-75884-P and RTI2018-098537-B-C22, and the Regional Governments of Aragón/FEDER 2014-2020 "*Building Europe from Aragón*" (groups E42_17R and E12_17R) and Principado de Asturias (FEDER: IDI/2018/000121) are gratefully acknowledged. The authors also acknowledge ALBA synchrotron for granting beamtime and the collaboration of the CLAESS beamline staff.

Appendix A. Supplementary data

Supplementary data to this article can be found online at https://doi.org/####.

References

[1] Lewis, N. S. & Nocera, D. G. Powering the planet: Chemical challenges in solar energy utilization. *Proceedings of the National Academy of Sciences, 103* (43*)* (2006) 15729-15735. doi:10.1073/pnas.0603395103

[2] Li, J., Güttinger, R., Moré, R., Song, F., Wan, W., Patzke, G. R. Frontiers of water oxidation: the quest for true catalysts. *Chemical Society Reviews, 46*(20) (2017) 6124-6147. doi:10.1039/C7CS00306D

[3] Cao, R., Lai, W., Du, P. Catalytic water oxidation at single metal sites. *Energy & Environmental Science, 5*(8) (2012) 8134-8157. doi:10.1039/C2EE21494F

[4] Llobet, A. *Molecular water oxidation catalysis: a key topic for new sustainable energy conversion schemes*. Chichester, UK, 2014: John Wiley & Sons.

[5] Sanchez Casalongue, H. G., Ng, M. L., Kaya, S., Friebel, D., Ogasawara, H. and Nilsson, A. In Situ Observation of Surface Species on Iridium Oxide Nanoparticles during the Oxygen Evolution Reaction. *Angewandte Chemie Internation Edition, 53*(28) (2014) 7169-7172. doi:10.1002/anie.201402311

[6] Qiu, T., Liang, Z., Guo, W., Gao, S., Qu, C., Tabassum, H., Zhang, H., Zhu, B., Zou, R., Shao-Horn, Y. Highly exposed ruthenium-based electrocatalysts from bimetallic metal-organic frameworks for overall water splitting. *Nano Energy, 58* (2019) 1-10. doi:10.1016/j.nanoen.2018.12.085

[7] Blakemore, J. D., Crabtree, R. H., Brudvig, G. W. Molecular catalysts for water oxidation. *Chemical Reviews, 115*(23) (2015) 12974-13005. doi:10.1021/ acs.chemrev.5b00122

[8] Concepcion, J. J., Jurss, J. W., Brennaman, M. K., Hoertz, P. G., Patrocinio, A. O. T., Murakami Iha, N. Y., Templeton, J. L., Meyer, T. J. Making oxygen with ruthenium

complexes. *Accounts of Chemical Research*, *42*(12) (2009) 1954-1965. doi:10.1021/ar9001526

[9] Fukuzumi, S., Jung, J., Yamada, Y., Kojima, T., Nam, W. Homogeneous and heterogeneous photocatalytic water oxidation by persulfate. *Chemistry: An Asian Journal*, *11*(8) (2006) 1138-1150. doi:10.1002/asia.201501329

[10] Zhan, S., Ahlquist, M. S. Dynamics and Reactions of Molecular Ru Catalysts at Carbon Nanotube–Water Interfaces. *Journal of the American Chemical Society*, *140*(24) (2018) 7498-7503. doi:10.1021/jacs.8b00433

[11] Matheu, R., Moreno-Hernandez, I. A., Sala, X., Gray, H. B., Brunschwig, B. S., Llobet, A., Lewis, N. S. Photoelectrochemical behavior of a molecular Ru-based water-oxidation catalyst bound to TiO_2-protected Si photoanodes. *Journal of the American Chemical Society*, *139*(33) (2017) 11345-11348. doi:10.1021/jacs.7b06800

[12] Schaetz, A., Zeltner, M., Stark, W. J. Carbon modifications and surfaces for catalytic organic transformations. *ACS Catalysis*, *2*(6) (2012) 1267-1284. doi: 10.1021/cs300014k

[13] deKrafft, K. E., Wang, C., Xie, Z., Su, X., Hinds, B. J., Lin, W. Electrochemical water oxidation with carbon-grafted iridium complexes. *ACS Applied Materials & Interfaces*, *4*(2) (2012) 608-613. doi:10.1021/am2018095

[14] Chen, W., Huang, L., Hu, J., Li, T., Jia, F., Song, Y. F. Connecting carbon nanotubes to polyoxometalate clusters for engineering high-performance anode materials. *Physical Chemistry Chemical Physics*, *16*(36) (2014) 19668-19673. doi:10.1039/C4CP03202K

[15] Nieto, J., Jiménez, M. V., Álvarez, P., Pérez-Mas, A. M., González, Z., Pereira, R., Sánchez-Page, B., Pérez-Torrente, J. J., Blasco, J., Subias, G., Blanco, M., Menéndez, R. Enhanced Chemical and Electrochemical Water Oxidation Catalytic Activity by Hybrid

Carbon Nanotube-Based Iridium Catalysts Having Sulfonate-Functionalized NHC ligands. *ACS Applied Energy Materials*, *2*(5) (2019) 3283-3296. doi:10.1021/acsaem.9b00137

[16] Hu, M., Yao, Z., Wang, X. Graphene-based nanomaterials for catalysis. *Industrial & Engineering Chemistry Research*, *56*(13) (2017) 3477-3502. doi:10.1021/acs.iecr.6b05048

[17] Fan, X., Zhang, G., Zhang, F. Multiple roles of graphene in heterogeneous catalysis. *Chemical Society Reviews*, *44*(10) (2015) 3023-3035. doi:10.1039/C5CS00094G

[18] Botas, C., Álvarez, P., Blanco, P., Granda, M., Blanco, C., Santamaría, R., Romasanta, L. J., Verdejo, R., López-Manchado M. A., Menéndez, R. Graphene materials with different structures prepared from the same graphite by the Hummers and Brodie methods. *Carbon*, *65* (2013) 156-164. doi: 10.1016/j.carbon.2013.08.009

[19] Botas, C., Álvarez, P., Blanco, C., Santamaría, R., Granda, M., Gutiérrez, M. D., Rodriguez-Reinoso, F., Menéndez, R. Critical temperatures in the synthesis of graphene-like materials by thermal exfoliation–reduction of graphite oxide. *Carbon*, *52* (2013) 476-485. doi:10.1016/j.carbon.2012.09.059

[20] Botas, C., Pérez-Mas, A. M., Álvarez, P., Santamaría, R., Granda, M., Blanco, C., Menéndez, R. Optimization of the size and yield of graphene oxide sheets in the exfoliation step. *Carbon*, *63* (2013) 576-578. doi:10.1016/j.carbon.2013.06.096

[21] Botas, C., Álvarez, P., Blanco, C., Santamaría, R., Granda, M., Ares, P., Rodríguez-Reinoso, F., Menéndez, R. The effect of the parent graphite on the structure of graphene oxide. *Carbon*, *50*(1) (2012) 275-282. doi: 10.1016/j.carbon.2011.08.045

[22] Peng, W., Han, G., Huang, Y., Cao, Y., Song, S. Insight the effect of crystallinity of natural graphite on the electrochemical performance of reduced graphene oxide. *Results in Physics*, *11* (2018) 131-137. doi: 10.1016/j.rinp.2018.08.055

[23] Wei, Y., Hu, X., Jiang, Q., Sun, Z., Wang, P., Qiu, Y., Liu, W. Influence of graphene oxide with different oxidation levels on the properties of epoxy composites. *Composites Science and Technology*, *161* (2018) 74-84. doi:10.1016/j.compscitech.2018.04.007

[24] Nakamura, J. The effect of a graphene support on the properties of Pt electrode catalysts in fuel cells. *Carbon*, *85* (2015) 443-444. doi: 10.1016/j.carbon.2014.12.019

[25] Kharisov, B. I., Kharissova, O. V., Vazquez Dimas, A., Gomez De La Fuente, I., Pena Mendez, Y. Graphene-supported coordination complexes and organometallics: properties and applications. *Journal of Coordination Chemistry*, *69*(7) (2016) 1125-1151. doi:10.1080/00958972.2016.1170817

[26] Axet, M. R., Durand, J., Gouygou, M., Serp, P. Surface coordination chemistry on graphene and two-dimensional carbon materials for well-defined single atom supported catalysts. *Advances in Organometallic Chemistry*, *71* (2019) 53-174.

[27] Blanco, M., Álvarez, P., Blanco, C., Jiménez, M. V., Fernández-Tornos, J., Pérez-Torrente, J. J., Oro, L. A., Menéndez, R. Effect of structural differences of carbon nanotubes and graphene based iridium-NHC materials on the hydrogen transfer catalytic activity. *Carbon*, *96* (2016) 66-74. doi:10.1016/j.carbon.2015.09.018

[28] Blanco, M., Álvarez, P., Blanco, C., Jiménez, M. V., Fernández-Tornos, J., Pérez-Torrente, J. J., Oro, L. A., Menéndez, R. Graphene–NHC–iridium hybrid catalysts built through–OH covalent linkage. *Carbon, 83* (2015) 21-31. doi: 10.1016/j.carbon.2014.11.016

[29] Bekhouche, M., Blum, L. J., Doumèche, B. Ionic Liquid-Inspired Cations Covalently Bound to Formate Dehydrogenase Improve its Stability and Activity in Ionic Liquids. *ChemCatChem*, *3*(5) (2011) 875-882. doi: 10.1002/cctc.201000390

[30] Uson, R., Oro, L. A., Cabeza, J. A., Bryndza, H. E., Stepro, M. P. Dinuclear methoxy, cyclooctadiene, and Barrelene complexes of rhodium (I) and Iridium (I). *Inorganic Syntheses*, *23* (1985) 126-130. doi: 10.1002/9780470132548.ch25

[31] Seah, M. P., Briggs, D. (Eds.). (1990). *Practical Surface Analysis: Auger and X-ray Photoelectron Spectroscopy*. New York. John Wiley & Sons. 2nd ed. vol.1, p.657.

[32] Elgrabli, D., Floriani, M., Abella-Gallart, S., Meunier, L., Gamez, C., Delalain, P., Rogerieux, F., Boczkowski, J., Lacroix, G. Biodistribution and clearance of instilled carbon nanotubes in rat lung. *Particle and Fibre Toxicology*, *5*(1) (2008) 20-33. doi:10.1186/1743-8977-5-20

[33] Simonelli, L., Marini, C., Olszewski, W., Avila Perez, M., Ramanan, N., Guilera, G., Cuartero, V., Klementiev, K. CLÆSS: The hard X-ray absorption beamline of the ALBA CELLS synchrotron. *Cogent Physics*, *3*(1) (2016) 1231987. doi:10.1080/23311940.2016.1231987

[34] Ravel, B., Newville, M. ATHENA, ARTEMIS, HEPHAESTUS: data analysis for X-ray absorption spectroscopy using IFEFFIT. *Journal of synchrotron radiation*, *12*(4) (2005) 537-541. doi:10.1107/S0909049505012719

[35] Rehr, J. J., Albers, R. C. Theoretical approaches to x-ray absorption fine structure. *Reviews of modern physics*, *72*(3) (2000) 621-654. doi: 10.1103/RevModPhys.72.621

[36] Ferrari, A. C., Robertson, J. Interpretation of Raman spectra of disordered and amorphous carbon. *Physical Review B*, *61*(20) (2000) 14095-14107. doi:10.1103/PhysRevB.61.14095

[37] Letsinger, R. L., Ogilvie, K. K. Use of p-nitrophenyl chloroformate in blocking hydroxyl groups in nucleosides. *Journal of Organic Chemistry*, *32*(2) (1967) 296-300. doi:10.1021/jo01288a011

[38] Oh, J. K., Drumright, R., Siegwart, D. J., Matyjaszewski, K. The development of microgels/nanogels for drug delivery applications. *Progress in Polymer Science*, *33*(4) (2008) 448-477. doi:10.1016/j.progpolymsci.2008.01.002

[39] Crotti, C., Farnetti, E., Filipuzzi, S., Stener, M., Zangrando, E., Moras, P. Evaluation of the donor ability of phenanthrolines in iridium complexes by means of synchrotron radiation photoemission spectroscopy and DFT calculations. *Dalton Transactions*, (1) (2007) 133-142. doi:10.1039/B613837C

[40] Blanco, M., Álvarez, P., Blanco, C., Jiménez, M. V., Fernández-Tornos, J., Pérez-Torrente, J. J., Oro, L. A., Menéndez, R. Enhanced hydrogen-transfer catalytic activity of iridium N-heterocyclic carbenes by covalent attachment on carbon nanotubes. *ACS Catalysis*, *3*(6) (2013) 1307-1317. doi: 10.1021/cs4000798

[41] Blanco, M.; Álvarez, P.; Blanco, C.; Jiménez, M.V.; Fernández-Tornos, J.; Pérez-Torrente, J.J.; Blasco, J.; Subías, G.; Cuartero, V.; Oro, L.A.; Menéndez, R. Effect of structural differences of carbon nanotubes and graphene based iridium-NHC materials on the hydrogen transfer catalytic activity. Carbon; 96 (2016) 66–74. doi: doi.org/10.1016/j.carbon.2015.09.018.

[42] Wang, C., Wang, J. L., Lin, W.. Elucidating molecular iridium water oxidation catalysts using metal–organic frameworks: A comprehensive structural, catalytic, spectroscopic, and kinetic study. *Journal of the American Chemical Society*, *134* (48), (2012) 19895-19908. doi:10.1021/ja310074j

Highlights

Hybrid materials resulting from the covalent attachment of Ir(I)-NHC complexes to thermally reduced graphene oxide materials are suitable electrocatalysts for water oxidation.

EXAFS analysis evidences that the properties of the parent graphite influence the iridium local structure in the hybrid materials.

The iridium local structure determines the electrocatalytic behavior in water oxidation.

Declaration of interests

☒ The authors declare that they have no known competing financial interests or personal relationships that could have appeared to influence the work reported in this paper.

☐The authors declare the following financial interests/personal relationships which may be considered as potential competing interests: